

Cite this: *Mater. Adv.*, 2024,  
5, 2120

# Metal–organic framework-derived hierarchical porous N/Co-doped carbon-supported sponge-like Pd–SnO<sub>2</sub> nanostructures for low-temperature CO oxidation†

Adewale K. Ipadeola,<sup>ab</sup> Ahmed Gamal,<sup>abc</sup> Belal Salah,<sup>ab</sup> Yassmin Ibrahim,<sup>ab</sup> Aboubakr M. Abdullah,<sup>id</sup> \*<sup>a</sup> Aderemi B. Haruna,<sup>c</sup> Kenneth I. Ozoemena,<sup>id</sup> \*<sup>c</sup> and Kamel Eid,<sup>id</sup> \*<sup>b</sup>

Metal–organic framework-derived porous N/Co-doped carbon (MOF-PNC) nanostructures-supported metal nanoparticles (NPs) are of great importance in multidisciplinary catalytic reactions; however, their catalytic performance toward low-temperature CO oxidation (CO<sub>Oxid</sub>) is rarely reported. Herein, a MOF-PNC-supported Pd–SnO<sub>2</sub> (Pd–SnO<sub>2</sub>/MOF-PNC) was synthesized *via* a microwave-irradiation (MW-IR), annealing, and chemical etching approach for thermal CO<sub>Oxid</sub>. The as-prepared Pd–SnO<sub>2</sub>/MOF-PNC had hierarchical porous sponge-like nanostructures composed of porous two-dimensional ultrathin nanosheets (NSs), co-doped with N/Co, with a high specific surface area (185.40 m<sup>2</sup> g<sup>−1</sup>) and pore volume (0.045 cm<sup>3</sup> g<sup>−1</sup>), and ornamented with Pd–SnO<sub>2</sub> NPs (7.79 ± 1.42 nm). These merits endowed the Pd–SnO<sub>2</sub>/MOF-PNC with excellent thermal catalytic CO<sub>Oxid</sub> activity at a low complete CO conversion temperature ( $T_{100}$  = 65.6 °C) compared to those of Pd(1%)-SnO<sub>2</sub>/MOF-PNC (165.2 °C), Pd–SnO<sub>2</sub> (199.1 °C), Pd/MOF-PNC (107.9 °C) and commercial Pd/C catalysts (201.2 °C), due to the augmented electronic interaction and synergy of Pd NPs with oxygen-rich SnO<sub>2</sub> supports and Co–N<sub>x</sub> active sites in MOF-PNC. Thus, coupling two supports (*i.e.*, SnO<sub>2</sub>/MOF-PNC) is more crucial for promoting the low-temperature CO<sub>Oxid</sub> activity of Pd NPs.

Received 7th October 2023,  
Accepted 5th December 2023

DOI: 10.1039/d3ma00819c

rsc.li/materials-advances

## Introduction

The global energy demand has increased substantially in the last few decades and is expected to continue to rise owing to the inevitable industrialization and civilization.<sup>1–3</sup> Limitless efforts to solve these issues lie in developing green energy technologies (*i.e.*, fuel cells,<sup>4</sup> batteries,<sup>5</sup> and water splitting<sup>6,7</sup>) and gas conversion reactions.<sup>8–10</sup> CO<sub>Oxid</sub> is formed during heterogeneous catalysis electrochemically,<sup>11,12</sup> or thermally,<sup>13–16</sup> but the latter is feasible for large-scale applications. Pd-based catalysts are among the most active catalysts for thermal CO<sub>Oxid</sub>, however, the high cost and earth-rarity of Pd are critical barriers.<sup>17</sup> Using metal oxide supports (SnO<sub>2</sub>, SiO<sub>2</sub>, Fe<sub>2</sub>O<sub>3</sub>, TiO<sub>2</sub>, and CeO<sub>2</sub>) could boost

the catalytic performance and stability, and reduce the cost.<sup>18,19</sup> Also, the electronic interaction and synergy of Pd with metal oxide supports enhances the activation/dissociation of CO/O<sub>2</sub> reactants and quickly desorbs intermediate species (*i.e.*, carbonate/formate) and products (*i.e.*, CO<sub>2</sub>). For instance, the Pd/MgO-h-BN catalyst showed a lower complete CO conversion temperature ( $T_{100}$  = 140 °C) than Pd/MgO (180 °C), but Pd/h-BN could not achieve  $T_{100}$ , due to the interaction of Pd with the MgO-h-BN support that enhanced the large amount of adsorbed O<sub>2</sub> and rapidly desorbed the intermediates.<sup>20</sup> Pd@SiO<sub>2</sub>-673-CeO<sub>2</sub> catalysts had great thermal CO<sub>Oxid</sub> at a lower  $T_{100}$  (92 °C) than Pd@SiO<sub>2</sub>-673 (130 °C), owing to the interaction of Pd with dual supports (*i.e.*, SiO<sub>2</sub> and CeO<sub>2</sub>).<sup>21</sup>

Unlike other supports, metal–organic framework-derived porous N/Co-doped carbon (MOF-PNC) nanostructures possess outstanding features (*i.e.* thermal/chemical stability and impressive surface area), and rich metal-N<sub>x</sub> active sites,<sup>22–24</sup> which are beneficial for uniform distribution and stabilization of Pd NPs.<sup>25–27</sup> In addition, they make Pd active sites readily accessible and maximize their utilization for thermal CO<sub>Oxid</sub>.<sup>28–30</sup> For instance, porous C-supported Cu/Cu<sub>2</sub>O nanojunctions derived from (Cu-BTC)-MOF had impressive CO<sub>Oxid</sub> activity achieved at  $T_{100}$

<sup>a</sup> Center for Advanced Materials, Qatar University, Doha 2713, Qatar.

E-mail: bakr@qu.edu.qa

<sup>b</sup> Gas Processing Center (GPC), College of Engineering, Qatar University, Doha 2713, Qatar. E-mail: kamel.eid@qu.edu.qa<sup>c</sup> Molecular Sciences Institute, School of Chemistry, University of the Witwatersrand, Private Bag 3, PO Wits, Johannesburg 2050, South Africa.

E-mail: Kenneth.ozoemena@wits.ac.za

† Electronic supplementary information (ESI) available. See DOI: <https://doi.org/10.1039/d3ma00819c>

(155–190 °C),<sup>31</sup> due to a high ratio of Cu metal phases (Cu<sup>0</sup>, Cu<sup>+</sup>, and Cu<sup>2+</sup>) and interaction with the porous C support. Noticeably, MOF-PNC-supported metal NPs are not emphasized enough, particularly using SnO<sub>2</sub> as a co-support, for thermal CO<sub>oxid</sub>, and their effect remains ambiguous.<sup>24,32–34</sup>

Herein, MOF-PNC-supported Pd–SnO<sub>2</sub> (Pd–SnO<sub>2</sub>/MOF-PNC) exhibited hierarchical porous sponge-like nanostructures comprising porous 2D ultrathin MOF-PNC NSs with abundant N/Co dopants, large specific surface area (185.40 m<sup>2</sup> g<sup>−1</sup>), and encapsulated spherical-like Pd–SnO<sub>2</sub> NPs (7.79 ± 1.42 nm). Coupling the properties of SnO<sub>2</sub> (*i.e.*, ease of adsorption and activation/dissociation of CO/O<sub>2</sub>) and the merits of MOF-PNC (*i.e.*, high surface area and rich metal-N<sub>x</sub> active sites) can ease CO oxidation on Pd at a low temperature and enhanced durability. The thermal CO<sub>oxid</sub> activities of Pd–SnO<sub>2</sub>/MOF-PNC, Pd(1%)–SnO<sub>2</sub>/MOF-PNC, Pd–SnO<sub>2</sub>, SnO<sub>2</sub>/MOF-PNC and Pd/MOF-PNC are benchmarked to commercial Pd/C catalysts in order to estimate the effect of the supports.

## Materials and methods

### Materials

Potassium tetrachloropalladate(II) (K<sub>2</sub>PdCl<sub>4</sub> ≥ 98%), tin(II) chloride dihydrate (SnCl<sub>2</sub>·2H<sub>2</sub>O ≥ 98%), cobalt(II) nitrate hexahydrate (Co(NO<sub>3</sub>)<sub>2</sub>·6H<sub>2</sub>O ≥ 94.5%), biphenyl-4,4'-dicarboxylic acid (BPDC ≥ 97%), ethylene glycol (EG ≥ 99.8%), triethyleamine (TEA ≥ 99.5%), dimethylformamide (DMF ≥ 99.8%), and commercial Pd/C catalyst (20 wt%) were purchased from Sigma-Aldrich Chemie GmbH (Munich, Germany).

### Preparation of MOF-derived porous Co/N-doped carbon (MOF-PNC)

MOF-PNC was synthesized by mixing Co(NO<sub>3</sub>)<sub>2</sub>·6H<sub>2</sub>O (0.44 g), BPDC (0.36 g), TEA (1.5 mL) and DMF (50 mL) under magnetic stirring at 25 °C, then microwave-irradiated at 600 W for 30 min.<sup>33</sup> The obtained precipitates were washed and dried in a vacuum oven at 60 °C, followed by annealing at 800 °C for 5 h. The obtained powder was soaked in an aqueous solution of HCl (3 M) for 24 h, washed, and dried to give MOF-PNC.

### Preparation of SnO<sub>2</sub>/MOF-PNC

SnO<sub>2</sub>/MOF-PNC was prepared by magnetically stirring SnCl<sub>2</sub>·2H<sub>2</sub>O (47.8 mg) in a mixture of EG and water (4:1 by volume); then, MOF-PNC (100 mg) was added and the mixture was microwave-irradiated at 600 W for 1 h. The resulting product (SnO<sub>2</sub>/MOF-PNC) was washed and dried at 80 °C for 4 h under vacuum.

### Preparation of Pd–SnO<sub>2</sub>/MOF-PNC

The as-prepared SnO<sub>2</sub>/MOF-PNC (100 mg) was mixed with K<sub>2</sub>PdCl<sub>4</sub> (61.35 mg) in EG (50 mL) at a pH of 12 with NaOH under magnetic stirring at 25 °C for 30 min, followed by microwave-irradiation at 600 W for 1 h (Anton Paar – Multiwave 3000).<sup>35</sup> Then, the mixture's pH was lowered to 3 using 0.1 M HNO<sub>3</sub>, and it was washed thoroughly with deionized H<sub>2</sub>O, and

dried at 80 °C for 4 h under a vacuum to afford Pd–SnO<sub>2</sub>/MOF-PNC. A similar method was used for the preparation of Pd(1%)–SnO<sub>2</sub>/MOF-PNC (1 wt% Pd loading) and Pd–SnO<sub>2</sub>.

### Preparation of Pd/MOF-PNC

Pd/MOF-PNC was prepared by mixing MOF-PNC (100 mg) with K<sub>2</sub>PdCl<sub>4</sub> (61.35 mg) in EG (50 mL) under magnetic stirring at 25 °C for 30 min and the pH was adjusted to 12 using NaOH solution (1 M). Then, the solution was placed in a microwave and irradiated at 600 W for 1 h.<sup>35</sup> Finally, the mixture's pH was decreased to 3 using 0.1 M HNO<sub>3</sub>, washed with deionized H<sub>2</sub>O, and dried at 80 °C for 4 h under vacuum.

### Characterisation

The morphology and composition analysis were conducted on a scanning electron microscope (SEM, Hitachi S-4800, Hitachi, Tokyo, Japan) and transmission electron microscope (TEM, TecnaiG220, FEI, Hillsboro, OR, USA) equipped with an energy dispersive spectrometer (EDS). The electronic structure and surface composition were carried out by X-ray photoelectron spectroscopy ((XPS) Ultra DLD XPS Kratos, Manchester, UK). The powder X-ray diffraction pattern (XRD) was measured on an X-ray diffractometer (X'Pert-Pro MPD, PANalytical Co., Almelo, Netherlands). The N<sub>2</sub>-physisorption isotherms were measured on a Quanta chrome Autosorb-1 analyzer (Quanta chrome Instrument Corporation). The Fourier transform infrared spectra (FT-IR) were recorded on a Thermo Nicolet Nexus 670 FT-IR spectrometer (Thermo Scientific).

### Thermal CO oxidation reaction

The thermal CO oxidation reaction was carried out in a fixed bed quartz tubular reactor connected to an online gas analyzer (Mass spectra, HIDEN ANALYTICAL the HPR-20 System) using 50 mg of each catalyst at the same Pd loading amount (20 wt%).<sup>36</sup> The catalyst was packed with quartz wool and fixed in the reactor and then pretreated at 200 °C (5 °C min<sup>−1</sup> heating ramp) under O<sub>2</sub> (5% in Ar) with a flow rate of 20 mL min<sup>−1</sup> for 1 h and subsequently under H<sub>2</sub> (5% in Ar) with a flow rate of 20 mL min<sup>−1</sup> for 1 h. After cooling to 25 °C, the catalyst was exposed to the gas mixture (O<sub>2</sub> (20%) + CO (4%) + Ar (76%)) at a flow rate of 20 mL min<sup>−1</sup> under heating to 300 °C (5 °C min<sup>−1</sup> ramping rate).<sup>36</sup> All the catalysts were subjected to the same treatment before the thermal CO oxidation. The percentage of CO conversion (%CO) was calculated using the following (eqn (1)):

$$\%CO = \left( \frac{CO_{in} - CO_{out}}{CO_{in}} \right) \times 100 \quad (1)$$

where CO<sub>in</sub> is the input amount of CO and CO<sub>out</sub> is the output amount of CO estimated from the mass spectra.

The CO temperature-programmed desorption (CO-TPD) was conducted by the initial pretreatment of each catalyst (50 mg) under Ar (50 mL min<sup>−1</sup> flow rate) at 300 °C (5 °C min<sup>−1</sup>) for 1 h in a Micromeritics ChemiSorb 2750 analyzer equipped with a thermal conductivity detector (TCD). After cooling to room temperature, the catalysts were exposed to (4% CO + 96% Ar)



at a flow rate of 30 mL min<sup>-1</sup> for 30 min under heating to 350 °C (5 °C min<sup>-1</sup>).<sup>36</sup>

The H<sub>2</sub> temperature-programmed reduction (H<sub>2</sub>-TPR) was measured by an initial pretreatment under Ar (50 mL min<sup>-1</sup>) at 300 °C (10 °C min<sup>-1</sup>) for 1 h and then exposed to (5% H<sub>2</sub> + 95% Ar) at a flow rate of 30 mL min<sup>-1</sup> under heating to 350 °C (5 °C min<sup>-1</sup>).<sup>36</sup>

The O<sub>2</sub> temperature-programmed oxidation (O<sub>2</sub>-TPO) was studied by initial treatment under Ar at a flow rate of 50 mL min<sup>-1</sup> at 300 °C (5 °C min<sup>-1</sup>) for 1 h and then exposed to (20% O<sub>2</sub> + 80% Ar) at a flow rate of 30 mL min<sup>-1</sup> under heating to 350 °C (20 °C min<sup>-1</sup>).

To get more insights into the thermal CO oxidation, the CO oxidation rate ( $r_{\text{CO}}$ ) of the catalysts was calculated at different CO conversion temperatures (10, 20, 50, and 80 °C) based on total gas flow ( $V_{\text{Gas}}$ ), initial concentration of CO ( $X_{\text{CO}}$ ), and molar weight of catalyst ( $M_{\text{Cat}}$ ) using eqn (2).

$$r_{\text{CO}} = \frac{X_{\text{CO}} \times V_{\text{Gas}}}{M_{\text{Cat}}} \quad (2)$$

The apparent activation energy ( $E_a$ ) was calculated at varied CO conversion (10–50%), based on the Arrhenius equation (eqn (3)) and the relationship between  $\ln r_{\text{CO}}$  and  $1/T$ .<sup>36</sup>

$$\ln r = \ln A - \frac{E_a}{RT} + a \ln[\text{CO}] + b \ln[\text{O}_2] \quad (3)$$

## Results and discussion

The Pd–SnO<sub>2</sub>/MOF-PNC was synthesized *via* the MW-I of Co(NO<sub>3</sub>)<sub>6</sub>·6H<sub>2</sub>O with biphenyl-4,4'-dicarboxylic acid (BPDC) and triethyleneamine (TEA) in dimethylformamide (DMF) solution to form a MOF, which was annealed and etched in HCl solution to afford MOF-PNC NSs (Fig. 1a).<sup>33</sup> This was followed by MW-I with the Sn precursor and then K<sub>2</sub>PdCl<sub>4</sub> in ethylene glycol (EG) to give Pd–SnO<sub>2</sub>/MOF-PNC.<sup>35</sup> The SEM of Pd–SnO<sub>2</sub>/MOF-PNC shows hierarchical porous sponge-like nanostructures (Fig. 1b), composed of porous 2D sheet-supported Pd NPs, with mean size (7.79 ± 1.42 nm), proved by TEM (Fig. 1c and d), which is important for stabilizing the Pd NPs against aggregation during the CO<sub>oxid</sub>. The lattice fringe (0.229 nm) of the Pd NPs is assigned to the {111} facet of face-center-cubic (fcc) Pd (Fig. 1e),<sup>35</sup> and the selected area electron diffraction pattern (SAED) reveals the typical rings of Pd (Fig. 1f).<sup>35</sup>

The EDX reveals the presence of Pd/Sn/Co/N/C/O with atomic contents (2.44/4.80/2.74/9.14/66.76/14.11 at%), indicating the successful formation of Pd/SnO<sub>2</sub> over MOF-PNC; however, Pd/MOF-PNC shows the existence of Pd/Co/N/C/O with contents (2.12/4.39/20.54/49.81/23.24 at%) (Fig. 1g) and uniform distribution mapped (Fig. S1, ESI†). Bulk and actual metal contents (Pd/Sn/Co (15.90/18.12/3.16 wt%)) in Pd–SnO<sub>2</sub>/MOF-PNC, (Pd/Co (17.70/11.24 wt%)) in Pd/MOF-PNC and (Pd (19.78 wt%)) in Pd/C are confirmed by ICP-OES (Table S1, ESI†). Meanwhile, the existence of Co in both catalysts is attributed to the partial etching by HCl, which is particularly important to coordinate with Pd–SnO<sub>2</sub> and provide additional active sites for thermal CO<sub>oxid</sub>. The SEM of Pd/MOF-PNC shows its porous sponge-like structure (Fig. S2a, ESI†), but lower porosity than Pd–SnO<sub>2</sub>/MOF-PNC, owing

to the possible gas release during the MW-I in the absence of the Sn precursor.

The distribution of Pd NPs (9.07 ± 1.75 nm), the lattice fringe (0.225 nm) for Pd{111} and SAED, but only Pd/Co/C distributed as mapped (Fig. S2b–f, ESI†). The Raman reveals the D- (1358.2 cm<sup>-1</sup>) and G-bands (1592.0 cm<sup>-1</sup>), but SnO<sub>2</sub> incorporation induced more defects in Pd–SnO<sub>2</sub>/MOF-PNC, proved by its higher  $I_{\text{D}}/I_{\text{G}}$  (2.01) than Pd/MOF-PNC (1.77) (Fig. S3a, ESI†).

The XRD of Pd–SnO<sub>2</sub>/MOF-PNC and Pd/MOF-PNC at 40°, 46° and 68° is assigned to {111}, {200} and {220} of fcc Pd along with the {002} facet of amorphous C at 26°, but Pd–SnO<sub>2</sub>/MOF-PNC has additional peaks of {101}, {200}, {211}, and {110} attributable to the tetragonal SnO<sub>2</sub> (Fig. 2a), compared to Pd/C (Fig. S4, ESI†).<sup>35</sup> The peak assigned to the C{002} facet in Pd–SnO<sub>2</sub>/MOF-PNC is broadened with higher full width at half maximum (FWHM) than Pd/MOF-PNC, due to the possible coordination of Pd–SnO<sub>2</sub> with Co–N<sub>x</sub> in MOF-PNC. This is also evidenced by the slight positive shifts of fcc Pd in Pd–SnO<sub>2</sub>/MOF-PNC and Pd/MOF-PNC relative to Pd/C, implying lattice contraction of Pd. Crystallite sizes (2.8 and 3.0 nm) from the Scherrer equation for Pd–SnO<sub>2</sub>/MOF-PNC and Pd/MOF-PNC, respectively.

The XPS survey of the catalysts displays the valence state of Pd 3d/Co 2p/C 1s/O 1s/N 1s, but Pd–SnO<sub>2</sub>/MOF-PNC showed additional spectra of Sn 3d (Fig. S3b, ESI†). The atomic contents of Pd (2.16 at%) in Pd–SnO<sub>2</sub>/MOF-PNC and 2.71 at% in Pd/MOF-PNC imply the coherent distribution of Pd on the surface, but the bulk metal contents are given by the ICP-OES (Table S1, ESI†), which is critical for providing enough active sites for thermal CO<sub>oxid</sub>. Pd 3d spectra of Pd–SnO<sub>2</sub>/MOF-PNC and Pd/MOF-PNC display the phases of Pd<sup>0</sup>, Pd<sup>2+</sup>, and Pd<sup>4+</sup> (Fig. 2b).<sup>35</sup> The ratio of Pd<sup>0</sup> to Pd<sup>2+</sup> in Pd–SnO<sub>2</sub>/MOF-PNC (0.62) was lower than Pd/MOF-PNC (0.77), due to the incorporation of metal oxide (*i.e.*, SnO<sub>2</sub>) signifying more Pd<sup>2+</sup> in the Pd–SnO<sub>2</sub>/MOF-PNC.<sup>35</sup>

The Pd–SnO<sub>2</sub>/MOF-PNC had a higher ratio of Pd<sup>2+</sup> than Pd/MOF-PNC, owing to its possible interaction with SnO<sub>2</sub> during the reduction process, which led to the partial oxidation of Pd to generate more active PdO<sub>x</sub> species and slightly decreased the d-band center of Pd, evidenced by the slight positive shift of Pd binding energies of Pd–SnO<sub>2</sub>/MOF-PNC than Pd/MOF-PNC (Table S2, ESI†). Norskov *et al.* suggested that a d-band center and d-bandwidth slightly below the Fermi level is optimal for CO chemisorption, so the reduced d-band center of Pd may allow strong interaction and possible poisoning and deactivation.<sup>37,38</sup> However, this did not happen in the case of Pd–SnO<sub>2</sub>/MOF-PNC, due to the promotional effect of Pd<sup>0</sup>/Pd–O<sub>x</sub> and their interfacial interaction with SnO<sub>2</sub> and Co/N-doped porous MOF-derived C. Notably, Norskov and co-workers reported the ability of promoters to balance the CO chemisorption on the metal surface and enhance its activity.<sup>37,38</sup> The C 1s spectra are assigned to sp<sup>3</sup>/sp<sup>2</sup> (C–C/C=C) and the C–N bond (Fig. 2c), but shifted positively in Pd–SnO<sub>2</sub>/MOF-PNC than Pd/MOF-PNC, due to the reduced electron density on C by the interaction with Pd–SnO<sub>2</sub>. The Sn 3d spectra display major Sn<sup>2+</sup> (3d<sub>5/2</sub> and 3d<sub>3/2</sub>) and minor Sn<sup>0</sup> (Fig. 2d). Meanwhile, Co 2p spectra show Co<sup>2+</sup> (3d<sub>3/2</sub> and 3d<sub>1/2</sub>) and Co<sup>0</sup> (Fig. 2e). The N 1s spectra are attributed to pyridinic, pyrrolic, and graphitic (Fig. 2f).





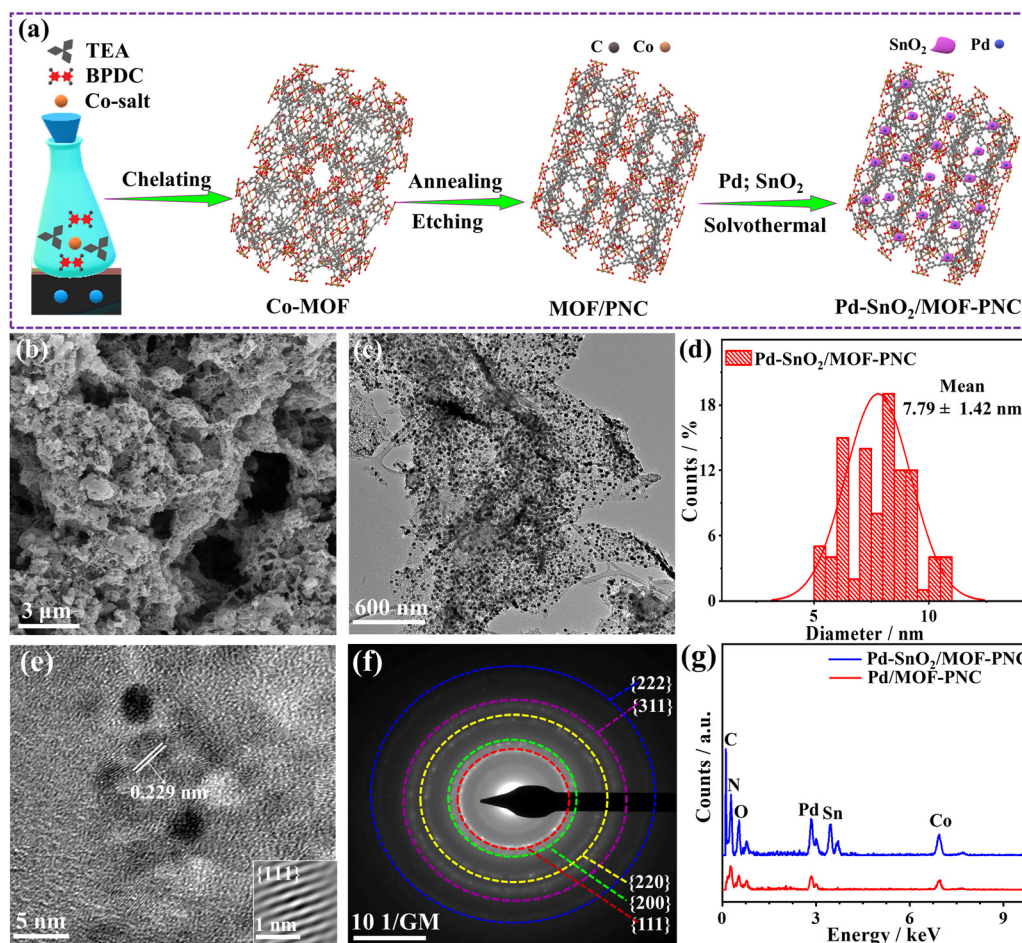


Fig. 1 (a) Schematic synthesis, (b) SEM, (c) TEM, (d) NPs size distribution, (e) HRTEM, (f) SAED of Pd-SnO<sub>2</sub>/MOF-PNC and (g) EDX of Pd-SnO<sub>2</sub>/MOF-PNC and Pd/MOF-PNC.

The BET-specific surface area of Pd-SnO<sub>2</sub>/MOF-PNC (185.40 m<sup>2</sup> g<sup>-1</sup>) is slightly higher than that of Pd/MOF-PNC (152.83 m<sup>2</sup> g<sup>-1</sup>), and Pd/C (107.91 m<sup>2</sup> g<sup>-1</sup>) (Fig. S5a-c, ESI<sup>†</sup>); meanwhile, the pore volume of Pd-SnO<sub>2</sub>/MOF-PNC (0.045 cm<sup>3</sup> g<sup>-1</sup>) was slightly higher than that of Pd/MOF-PNC (0.030 cm<sup>3</sup> g<sup>-1</sup>), and Pd/C (0.012 m<sup>3</sup> g<sup>-1</sup>), in addition to their multiple pore size range (2–110 nm) with mean pore sizes of 66.78, 56.54, and 12.31 nm for Pd-SnO<sub>2</sub>/MOF-PNC, Pd/MOF-PNC, and Pd/C, respectively (Fig. S5d-f, ESI<sup>†</sup>).

The thermal CO<sub>oxid</sub> shows typical light-off curves for the conversion of CO to CO<sub>2</sub> at heating temperatures (25–300 °C) and atmospheric pressure, but a superior activity on Pd-SnO<sub>2</sub>/MOF-PNC than Pd/MOF-PNC, and Pd/C (Fig. 3a).<sup>39,40</sup> The T<sub>100</sub> of Pd-SnO<sub>2</sub>/MOF-PNC (65.6 °C) is lower than that of Pd/MOF-PNC (107.9 °C) by 42.3 °C and Pd/C (201.2 °C) by 135.6 °C. This is due to the electronic and synergistic interaction of Pd<sup>0</sup>/Pd-O<sub>x</sub> active sites with oxygen-enriched SnO<sub>2</sub>, Co-N<sub>x</sub> and MOF-PNC, which optimizes CO + O<sub>2</sub> adsorption/activation and desorption of CO<sub>2</sub> at low temperatures.

Thus, Pd-SnO<sub>2</sub>/MOF-PNC has higher CO<sub>oxid</sub> kinetics than Pd/MOF-PNC, and Pd/C, owing to its capacity to oxidize CO at all applied temperatures (Fig. 3b), *i.e.*, 50% of CO to CO<sub>2</sub>

(T<sub>50</sub> = 58.4 °C) on Pd-SnO<sub>2</sub>/MOF-PNC was lower than Pd/MOF-PNC (99.9 °C) and Pd/C (186 °C). So, Pd-SnO<sub>2</sub>/MOF-PNC completely oxidizes CO within only 13.12 min compared to Pd/MOF-PNC (21.58 min) and Pd/C (40.24 min) (Fig. 3c). The CO<sub>oxid</sub> activity of Pd-SnO<sub>2</sub>/MOF-PNC was superior to previously reported Pd-based catalysts, *i.e.*, Pd/CeSn, Pd@SiO<sub>2</sub>/TiO<sub>2</sub>, Pd@CeO<sub>2</sub>, Pd/MgO, (Pd@SiO<sub>2</sub>-673-CeO<sub>2</sub> (92 °C)),<sup>21</sup> Pd/MgO-h-BN (140 °C),<sup>20</sup> Cu/Cu<sub>2</sub>O-500 nanojunctions (155 °C),<sup>31</sup> Pd/Cu/gC<sub>3</sub>N<sub>4</sub>NTs (154 °C),<sup>41</sup> Pd-Cu/gC<sub>3</sub>N<sub>4</sub>NWs (149 °C),<sup>42</sup> and Au/Pd/gC<sub>3</sub>N<sub>4</sub>NFs (149 °C)<sup>43</sup> (Table S3, ESI<sup>†</sup>). The T<sub>100</sub> of Pd-SnO<sub>2</sub>/MOF-PNC (65.6 °C) is among the lowest values reported for Pd-based catalysts as far as we found. The CO<sub>oxid</sub> rate (r<sub>CO</sub>) of Pd-SnO<sub>2</sub>/MOF-PNC was 1.95 and 2.15 times that of Pd/MOF-PNC and Pd/C, respectively (Fig. 3d), indicating maximum utilization of Pd active sites in Pd-SnO<sub>2</sub>/MOF-PNC, due to its greater porosity, which makes Pd active sites more accessible during CO<sub>oxid</sub>.

This is further seen in the lower activation energy (E<sub>a</sub> = 69.5 kJ mol<sup>-1</sup>) of Pd-SnO<sub>2</sub>/MOF-PNC than Pd/MOF-PNC (74.1 kJ mol<sup>-1</sup>) and Pd/C (89.2 kJ mol<sup>-1</sup>) (Fig. 3e). The CO<sub>oxid</sub> stability of Pd-SnO<sub>2</sub>/MOF-PNC at 65.6 °C was shown by a time-on-stream (TOS) for 108 h (Fig. 3f), which reveals excellent durability with insignificant loss in T<sub>100</sub>. The stability of



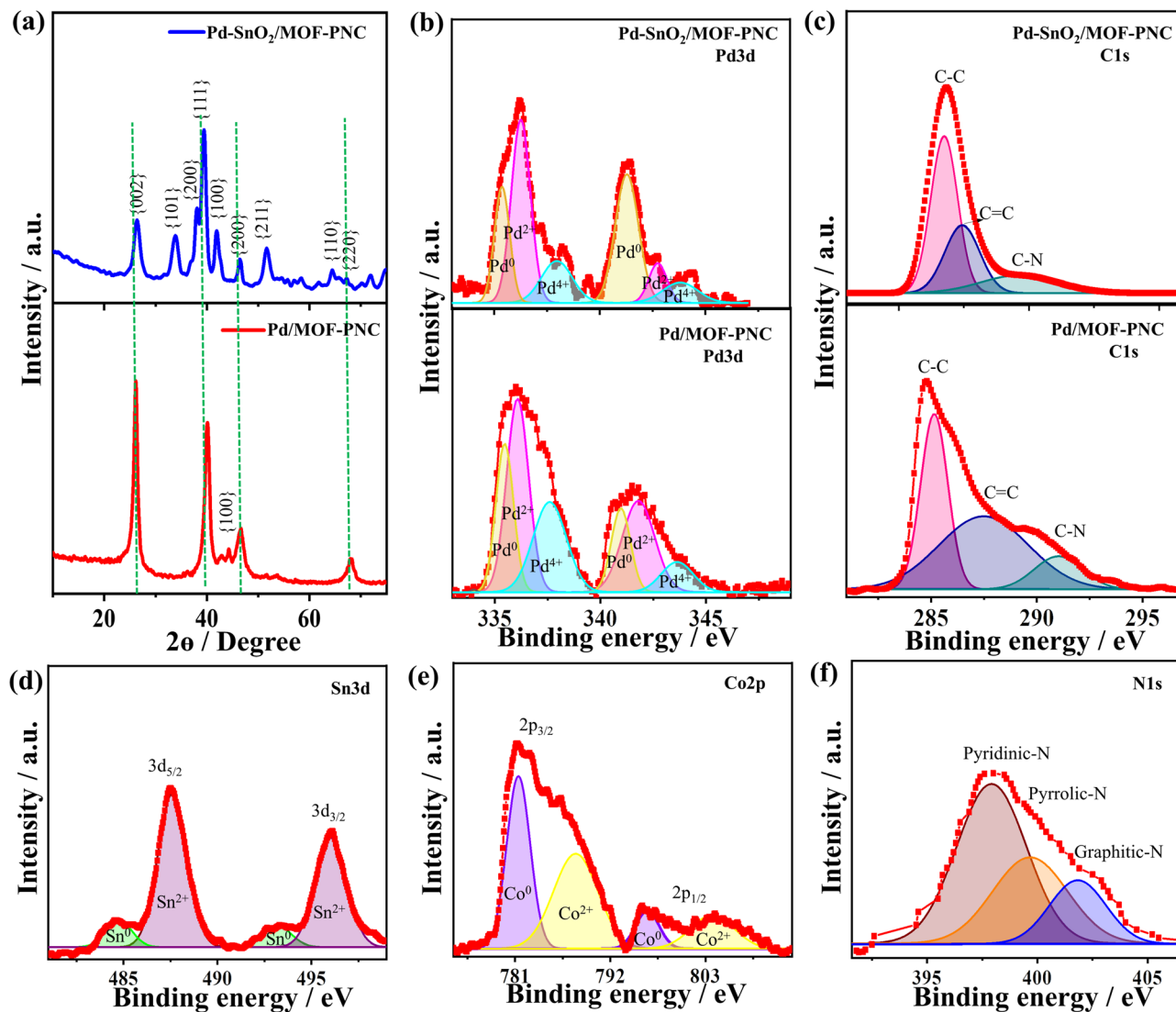


Fig. 2 (a) XRD, and high-resolution XPS (b) Pd 3d, (c) C 1s (d) Sn 3d, (e) Co 2p and (f) N 1s of Pd-SnO<sub>2</sub>/MOF-PNC and Pd/MOF-PNC. The green lines in (a) refer to the positions of pure Pd NPs on C, which were taken from the JCPDS database.

Pd-SnO<sub>2</sub>/MOF-PNC is further provided by TEM, which displayed the good dispersion of Pd nanoparticles over SnO<sub>2</sub>/MOF-PNC without any obvious aggregation, indicating the architecture durability (Fig. S6a, ESI†). The XPS full-scan showed the presence of C 1s, Pd 3d, Co 2p, O 1s, N 1s, and Sn 3d without significant degradation for Pd (2.13 at%), implying compositional stability (Fig. S6b, ESI†). The BET maintained the same isotherm adsorption/desorption features before stability with an inferior loss in the surface area and pore volume (Fig. S6c and d, ESI†). This implies the reservation of the physiochemical properties of Pd-SnO<sub>2</sub>/MOF-PNC after the durability test, as also proved by measuring the CO<sub>Oxid</sub> after the stability test, which displayed a minimal loss in the T<sub>100</sub> (only 5 °C) (Fig. S4b, ESI†).

The active sites and CO<sub>2</sub> production rate of Pd-SnO<sub>2</sub>/MOF-PNC are proved by its higher turnover number (TON = 14.8 μmol g<sub>Cat</sub><sup>-1</sup>) and turnover frequency (TOF = 61.97 h<sup>-1</sup>) relative to Pd/MOF-PNC (11.5 μmol g<sub>Cat</sub><sup>-1</sup>; 45.75 h<sup>-1</sup>) and Pd/C

(7.86 μmol g<sub>Cat</sub><sup>-1</sup>; 31.49 h<sup>-1</sup>) (Fig. 4a and b). The recyclability of Pd-SnO<sub>2</sub>/MOF-PNC reveals that the catalyst remained active for 5 consecutive cycles with no degradation. The CO-TPD gave sharp peaks for Pd-SnO<sub>2</sub>/MOF-PNC (74.5 °C) and Pd/MOF-PNC (72.6 °C), compared to a broad peak for Pd/C (174.2 °C) (Fig. 5a). This implies more accessible Pd active sites in Pd-SnO<sub>2</sub>/MOF-PNC and its capacity to adsorb/oxidize CO at a lower temperature due to the presence of an oxygen-rich SnO<sub>2</sub> support, higher surface area, and abundant active sites.<sup>36</sup>

The O<sub>2</sub>-TPO displays a sharp oxygen-uptake peak on Pd-SnO<sub>2</sub>/MOF-PNC (66.8 °C) relative to broad peaks on Pd/MOF-PNC (116.3 °C) and Pd/C (197.6 °C) (Fig. 5b), implying ease of O<sub>2</sub> adsorption (O<sub>ads</sub>) on Pd-SnO<sub>2</sub>/MOF-PNC, due to the interfacial interaction of Pd with SnO<sub>2</sub> and MOF-PNC. This leads to rapid turnover of the adsorbed CO/O<sub>2</sub>, which is important for inducing a reaction between the active O<sub>ads</sub> and CO<sub>ad</sub> on the Pd surface to allow quick CO<sub>Oxid</sub> kinetics.<sup>36</sup> Also, the oxygenated species (*i.e.*, SnO<sub>2</sub>) in Pd-SnO<sub>2</sub>/MOF-PNC enables a lower energy barrier for



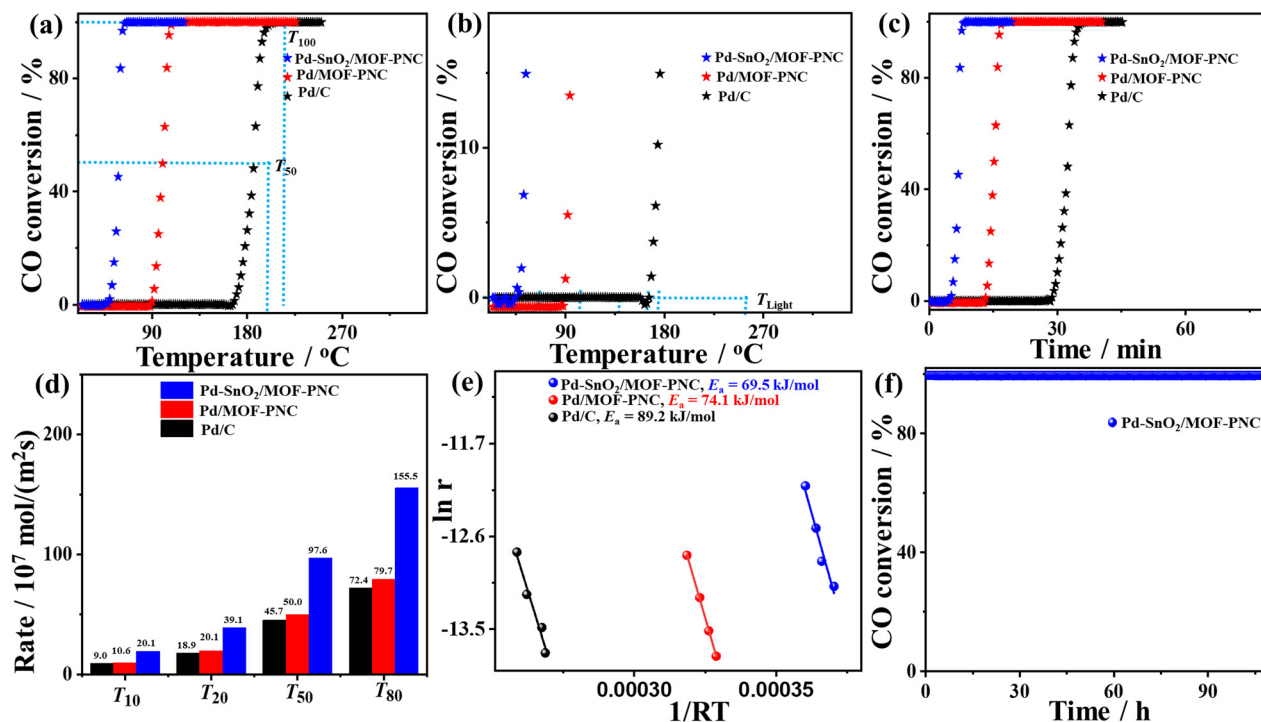


Fig. 3 (a, b) Temperature-dependent CO conversion, (c) time-dependent CO conversion, (d) rate at different CO conversion temperatures, (e) Arrhenius plots, and (f) time on stream (TOS) of Pd-SnO<sub>2</sub>/MOF-PNC, Pd/MOF-PNC, and Pd/C.

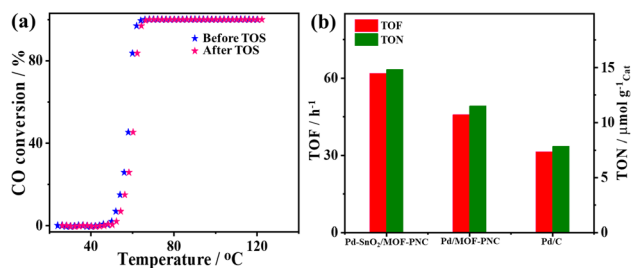
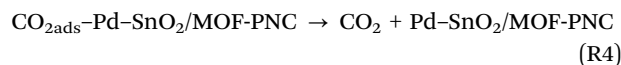
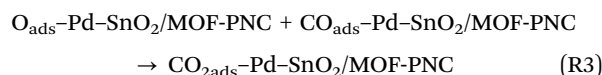
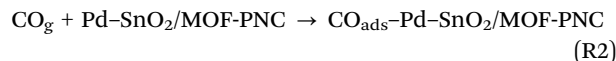
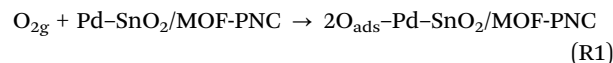


Fig. 4 (a) Temperature of CO conversion before and after the TOS test and repetitive CO conversion after H<sub>2</sub>-TPR and O<sub>2</sub>-TPO of Pd-SnO<sub>2</sub>/MOF-PNC. (b) Turnover number (TON) and turnover frequency (TOF) of Pd-SnO<sub>2</sub>/MOF-PNC, Pd/MOF-PNC and Pd/C.

CO/O<sub>2</sub> uptake/activation, thereby accelerating the complete CO<sub>Oxid</sub> kinetics.<sup>24,33</sup> The H<sub>2</sub>-TPR confirms the reducibility of the catalysts,<sup>36</sup> where Pd-SnO<sub>2</sub>/MOF-PNC, Pd/MOF-PNC, and Pd/C show a broad H<sub>2</sub> adsorption at 62.3, 184.1, and 199.9 °C, respectively, which implies that Pd-SnO<sub>2</sub>/MOF-PNC got reduced fast, owing to the interaction of SnO<sub>2</sub>, Pd<sup>2+</sup>, and Co<sup>2+</sup> (Fig. 5c). This may serve as evidence for its exposed metal active sites.

The H<sub>2</sub>-TPR, O<sub>2</sub>-TPO, and CO-TPD reveal that coupled Pd, SnO<sub>2</sub>, and MOF-PNC enhance the CO redox properties and CO<sub>Oxid</sub> activity of Pd-SnO<sub>2</sub>/MOF-PNC. Hence, the CO<sub>Oxid</sub> mechanism on Pd-SnO<sub>2</sub>/MOF-PNC could follow Langmuir-Hinshelwood,<sup>36</sup> *i.e.*, co-adsorption of CO/O<sub>2</sub> on Pd-SnO<sub>2</sub>/MOF-PNC, followed by dissociation of O<sub>2</sub> to form O lattice and O adsorbed (O<sub>ads</sub>) (eqn (R1) and (R2)), which then oxidizes CO<sub>ads</sub> to CO<sub>2ads</sub> (*i.e.*, the rate determining step (eqn (R3))) and CO<sub>2</sub> desorbed from Pd-SnO<sub>2</sub>/MOF-PNC (eqn (R4)).



To investigate the effect of Pd nanoparticles loaded with a lower content (*i.e.*, 1 wt%) decorated on SnO<sub>2</sub>/MOF-PNC, Pd(1%)-SnO<sub>2</sub>/MOF-PNC was prepared and tested for thermal CO oxidation, which showed significantly higher T<sub>100</sub> (165.2 °C) than Pd-SnO<sub>2</sub>/MOF-PNC (65.6 °C) (Fig. S7a, ESI†). Meanwhile, in the absence of Pd nanoparticles, SnO<sub>2</sub>/MOF-PNC could not attain T<sub>100</sub> even at 300 °C, implying that Pd is the main active site for the thermal CO oxidation. Also, to get more insights into the effect of the support, Pd-SnO<sub>2</sub> was examined for CO<sub>Oxid</sub> and achieved T<sub>100</sub> (199.1 °C) which was greater than Pd-SnO<sub>2</sub>/MOF-PNC (65.6 °C) and even Pd/MOF-PNC (107.9 °C) (Fig. S7a-c, ESI†), which indicates that using a co-support of SnO<sub>2</sub>/MOF-PNC is crucial for promoting the CO<sub>Oxid</sub> activity and kinetics as further seen in the lower rate (*r*<sub>CO</sub>) of Pd-SnO<sub>2</sub> than that of Pd-SnO<sub>2</sub>/MOF-PNC, and Pd(1%)-SnO<sub>2</sub>/MOF-PNC (Fig. S7d, ESI†). Also, the estimated E<sub>a</sub> of Pd-SnO<sub>2</sub> was greater than that of Pd(1%)-SnO<sub>2</sub>/MOF-PNC, Pd/MOF-PNC, and Pd-SnO<sub>2</sub>/MOF-PNC (Fig. S7e, ESI†). These results clarify the importance of combining mixed Pd phases (Pd<sup>0</sup>/Pd-O<sub>x</sub>) and an oxygen-rich SnO<sub>2</sub> support for excellent CO<sub>Oxid</sub> activity as





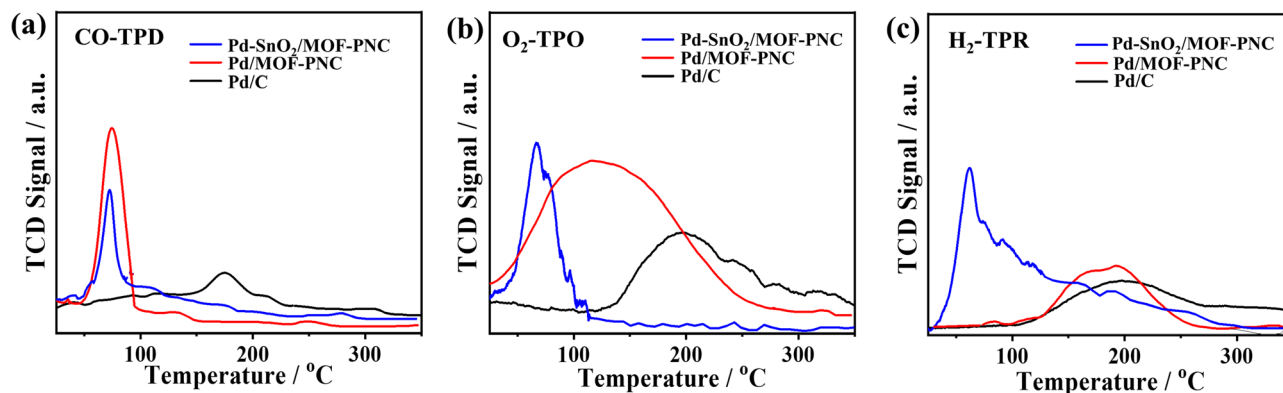


Fig. 5 (a) CO-temperature-programmed desorption (CO-TPD), (b) O<sub>2</sub>-temperature-programmed oxidation (O<sub>2</sub>-TPO), and (c) H<sub>2</sub>-temperature-programmed reduction (H<sub>2</sub>-TPR) of Pd-SnO<sub>2</sub>/MOF-PNC, Pd/MOF-PNC and Pd/C.

shown by low  $T_{100}$ , but high kinetics, TON and TOF of Pd-SnO<sub>2</sub>/MOF-PNC. Thus, coupling Pd with a metal oxide support is preferred for promoting the CO<sub>Oxid</sub>, due to the optimal CO/O<sub>2</sub> adsorption and ease of activation/dissociation at low temperatures.

## Conclusion

In brief, hierarchical porous sponge-like Pd-SnO<sub>2</sub>/MOF-PNC was prepared by the MW-I, annealing, and chemical etching approach to initially form MOF-PNC, mixed with SnO<sub>2</sub> and Pd and then MW-I. Pd-SnO<sub>2</sub>/MOF-PNC comprises porous 2D ultrathin MOF-PNC NSs with monodispersed Pd-SnO<sub>2</sub> NPs ( $7.79 \pm 1.42$  nm), a large specific surface area ( $185.40 \text{ m}^2 \text{ g}^{-1}$ ), and pore volume ( $0.045 \text{ cm}^3 \text{ g}^{-1}$ ). Thus, the CO<sub>Oxid</sub> at  $T_{100}$  of Pd-SnO<sub>2</sub>/MOF-PNC ( $65.6 \text{ }^\circ\text{C}$ ) was lower than those of Pd/MOF-PNC ( $107.9 \text{ }^\circ\text{C}$ ), Pd(1%)-SnO<sub>2</sub>/MOF-PNC ( $165.2 \text{ }^\circ\text{C}$ ), Pd-SnO<sub>2</sub> ( $199.1 \text{ }^\circ\text{C}$ ), and Pd/C ( $201.2 \text{ }^\circ\text{C}$ ), and also superior to most previously reported Pd-based catalysts. This originated from the electronic interaction and synergism of Pd NPs with oxygen-rich SnO<sub>2</sub> supports and Co-N<sub>x</sub> active sites in MOF-PNC to deliver low energy barriers and high kinetics. These results indicate that using two supports, SnO<sub>2</sub>/MOF-PNC is preferred for promoting the thermal CO<sub>Oxid</sub> activity of Pd NPs.

## Conflicts of interest

We declare no conflicts of interest.

## Acknowledgements

This work was supported by the Qatar University High Impact Internal Grant (QUHI-CAM-22/23-550) and the DSI-NRF-Wits SARCHI Chair in Materials Electrochemistry and Energy Technologies (MEET) (UID No.132739).

## References

- K. Eid, Q. Lu, S. Abdel-Azeim, A. Soliman, A. M. Abdullah, A. M. Abdelgwad, R. P. Forbes, K. I. Ozoemena, R. S. Varma and M. F. Shibl, *J. Mater. Chem. A*, 2022, **10**, 1965–1975.
- K. Liu, P. Cao, W. Chen, C. I. Ezech, Z. Chen, Y. Luo, Q. Liu, H. Zhao, Z. Rui and S. Gao, *Mater. Adv.*, 2022, **3**, 1359–1400.
- B. Salah, A. Abdelgwad, Q. Lu, A. K. Ipadeola, R. Luque and K. Eid, *Green Chem.*, 2023, **25**, 6032–6040.
- K. Timmo, M. Pilvet, K. Muska, M. Altosaar, V. Mikli, R. Kaupmees, R. Josepson, J. Krustok, M. Grossberg-Kuusik and M. Kauk-Kuusik, *Mater. Adv.*, 2023, **4**, 4509–4519.
- J. Saengkaew, T. Kameda and S. Matsuda, *Mater. Adv.*, 2023, **4**, 4417–4424.
- Q. Lu, J. Li, K. Eid, X. Gu, Z. Wan, W. Li, R. S. Al-Hajri and A. M. Abdullah, *J. Electroanal. Chem.*, 2022, **916**, 116361.
- P. Aggarwal, B. Singh and A. Paul, *Mater. Adv.*, 2023, **4**, 4377–4389.
- K. Eid, A. Gamal and A. M. Abdullah, *Green Chem.*, 2023, **25**, 1276–1310.
- S. Ghosh, A. Modak, A. Samanta, K. Kole and S. Jana, *Mater. Adv.*, 2021, **2**, 3161–3187.
- J. Marti-Rujas, *Mater. Adv.*, 2023, **4**, 4333–4343.
- K. Eid, Y. H. Ahmad, H. Yu, Y. Li, X. Li, S. Y. AlQaradawi, H. Wang and L. Wang, *Nanoscale*, 2017, **9**, 18881–18889.
- A. K. Ipadeola, A. B. Haruna, A. M. Abdullah, M. F. Shibl, D. Ahmadalie, K. I. Ozoemena and K. Eid, *Catal. Today*, 2023, 114178.
- Y. A. May, S. Wei, W.-Z. Yu, W.-W. Wang and C.-J. Jia, *Langmuir*, 2020, **36**, 11196–11206.
- Q. Xiao, S. Wei, W.-W. Wang and C.-J. Jia, *Langmuir*, 2021, **37**, 3270–3280.
- C. Miao, L. Zhang, W. Xie, L. Liang, S. Chen, Y. Zhang and J. Ouyang, *Mater. Adv.*, 2022, **3**, 232–244.
- B. Szcześniak, J. Choma and M. Jaroniec, *Mater. Adv.*, 2021, **2**, 2510–2523.
- X. Chen, L. P. Granda-Marulanda, I. T. McCrum and M. Koper, *Nat. Commun.*, 2022, **13**, 1–11.
- C. R. Zanata, A. C. Gaiotti, L. R. Sandim, C. A. Martins, L. M. Pinto, M. J. Giz and G. A. Camara, *J. Electroanal. Chem.*, 2021, **886**, 115149.
- H. Ahmad and M. K. Hossain, *Mater. Adv.*, 2022, **3**, 859–887.
- L. Li, X. Liu, H. He, N. Zhang, Z. Liu and G. Zhang, *Catal. Today*, 2019, **332**, 214–221.
- Y. Xu, J. Ma, Y. Xu, L. Xu, L. Xu, H. Li and H. Li, *RSC Adv.*, 2013, **3**, 851–858.



- 22 Y. Aoyama, H. Kobayashi, T. Yamamoto, T. Toriyama, S. Matsumura, M. Haneda and H. Kitagawa, *Chem. Commun.*, 2020, **56**, 3839–3842.
- 23 A. K. Ipadeola, A. Gamal, A. M. Abdullah, A. B. Haruna, K. I. Ozoemena and K. Eid, *Catal. Sci. Technol.*, 2023, **13**, 4873–4882.
- 24 A. K. Ipadeola, K. Eid, A. M. Abdullah and K. I. Ozoemena, *Langmuir*, 2022, **38**, 11109–11120.
- 25 Y. Xue, G. Zhao, R. Yang, F. Chu, J. Chen, L. Wang and X. Huang, *Nanoscale*, 2021, **13**, 3911–3936.
- 26 J. Liu, T. A. Goetjen, Q. Wang, J. G. Knapp, M. C. Wasson, Y. Yang, Z. H. Syed, M. Delferro, J. M. Notestein and O. K. Farha, *Chem. Soc. Rev.*, 2022, **51**, 1045–1097.
- 27 M. Sadakiyo, *Nanoscale*, 2022, **14**, 3398–3406.
- 28 Q. Liang, Z. Zhao, J. Liu, Y.-C. Wei, G.-Y. Jiang and A.-J. Duan, *Acta Phys.-Chim. Sin.*, 2014, **30**, 129–134.
- 29 Y. Hu, X. Song, Q. Zheng, J. Wang and J. Pei, *RSC Adv.*, 2019, **9**, 9962–9967.
- 30 G. Zhong, D. Liu and J. Zhang, *J. Mater. Chem. A*, 2018, **6**, 1887–1899.
- 31 R. Zhang, L. Hu, S. Bao, R. Li, L. Gao, R. Li and Q. Chen, *J. Mater. Chem. A*, 2016, **4**, 8412–8420.
- 32 M. Hao, M. Qiu, H. Yang, B. Hu and X. Wang, *Sci. Total Environ.*, 2021, **760**, 143333.
- 33 A. K. Ipadeola, K. Eid, A. M. Abdullah, R. S. Al-Hajri and K. I. Ozoemena, *Nanoscale Adv.*, 2022, **4**, 5044–5055.
- 34 X. Wang, W. Zhong and Y. Li, *Catal. Sci. Technol.*, 2015, **5**, 1014–1020.
- 35 A. K. Ipadeola, P. V. Mwonga, S. C. Ray, R. R. Maphanga and K. I. Ozoemena, *ChemElectroChem*, 2020, **7**, 4562–4571.
- 36 K. Eid, M. H. Sliem, M. Al-Ejji, A. M. Abdullah, M. Harfouche and R. S. Varma, *ACS Appl. Mater. Interfaces*, 2022, **14**, 40749–40760.
- 37 B. Hammer, O. H. Nielsen and J. Nørskov, *Catal. Lett.*, 1997, **46**, 31–35.
- 38 B. Hammer, Y. Morikawa and J. K. Nørskov, *Phys. Rev. Lett.*, 1996, **76**, 2141.
- 39 Y. Fang, X. Chi, L. Li, J. Yang, S. Liu, X. Lu, W. Xiao, L. Wang, Z. Luo and W. Yang, *ACS Appl. Mater. Interfaces*, 2020, **12**, 7091–7101.
- 40 W. Li, Q. Ge, X. Ma, Y. Chen, M. Zhu, H. Xu and R. Jin, *Nanoscale*, 2016, **8**, 2378–2385.
- 41 K. Eid, M. H. Sliem, K. Jlassi, A. S. Eldesoky, G. G. Abdo, S. Y. Al-Qaradawi, M. A. Sharaf, A. M. Abdullah and A. A. Elzatahry, *Inorg. Chem. Commun.*, 2019, **107**, 107460.
- 42 K. Eid, Y. H. Ahmad, A. T. Mohamed, A. G. Elsafy and S. Y. Al-Qaradawi, *Catalysts*, 2018, **8**, 411.
- 43 K. Eid, M. H. Sliem, A. S. Eldesoky, H. Al-Kandari and A. M. Abdullah, *Int. J. Hydrogen Energy*, 2019, **44**, 17943–17953.

